






Signatures of coupling between spin waves and Dirac fermions in YbMnBi₂A. Sapkota ^{1,*}, L. Classen,^{1,2,†} M. B. Stone ³, A. T. Savici ³, V. O. Garlea,³ Aifeng Wang,^{1,‡}
J. M. Tranquada ¹, C. Petrovic,¹ and I. A. Zaliznyak ^{1,§}¹*Condensed Matter Physics and Materials Science Division, Brookhaven National Laboratory, Upton, New York 11973, USA*²*School of Physics and Astronomy, University of Minnesota, Minneapolis, Minnesota 55415, USA*³*Neutron Scattering Division, Oak Ridge National Laboratory, Oak Ridge, Tennessee 37831, USA*

(Received 26 August 2019; published 24 January 2020)

We present inelastic neutron scattering measurements of magnetic excitations in YbMnBi₂, which reveal features consistent with a direct coupling of magnetic excitations to Dirac fermions. In contrast with the large broadening of magnetic spectra observed in antiferromagnetic metals such as the iron pnictides, here the spin waves exhibit a small but resolvable intrinsic width, consistent with our theoretical analysis. The subtle manifestation of spin-fermion coupling is a consequence of the Dirac nature of the conduction electrons, including the vanishing density of states near the Dirac points. Accounting for the Dirac fermion dispersion specific to YbMnBi₂ leads to particular signatures, such as the nearly wave-vector-independent damping observed in the experiment.

DOI: [10.1103/PhysRevB.101.041111](https://doi.org/10.1103/PhysRevB.101.041111)

Dirac and Weyl materials exhibit many exotic and novel quantum phenomena that are both of fundamental and potential technological interest [1–4]. This class of materials encompasses a wide range of condensed matter systems including graphene, *d*-wave superconductors, and topological insulators and semimetals [1]. In these materials, the linear variation of energy as a function of wave vector about a Dirac node is a universal feature that leads to novel behaviors such as suppression of backscattering, high carrier mobility, impurity-induced resonant states, spin-polarized transport, and the unusual quantum Hall effect [1–6]. Furthermore, the interaction of these low-energy Dirac/Weyl fermions with other degrees of freedom leads to novel physics with a technological potential [2,7,8]. Hence, understanding the coupling of Dirac fermions with other quantum excitations, such as spin waves, is a topic of great current interest.

From this perspective, 112 ternary bismuthides (*R*, *A*)MnBi₂ (*R* = rare earth, *A* = alkaline earth: Ca, Sr) represent a particularly interesting family where both magnetism and Dirac fermions coexist, providing a platform to study their interplay [3,4,9–11]. In these materials, the Dirac bands and the magnetic order are associated with distinct square-net layers: conducting Bi layers and magnetic MnBi layers separated by layers of *R*, *A*, as shown in Fig. 1(a) of Ref. [12]. While indirect experimental evidence of a coupling between conduction electrons and magnetic Mn ions is provided by the impact of the magnetic order on electrical transport in CaMnBi₂ [11,13], inelastic neutron scattering measurements on Sr/CaMnBi₂ found spin waves without any

evidence of strong damping due to particle-hole excitations of the type seen in compounds such as CaFe₂As₂ [14].

RMnBi₂ systems were suggested as possible candidates where the coupling of Dirac fermions with spins could be significant. EuMnBi₂ and YbMnBi₂ are two such recently discovered materials [12]. YbMnBi₂ is particularly interesting because of its possible link with type-II Weyl physics with broken time-reversal symmetry [15–17]. In addition, the ferromagnetic stacking of Mn moments along the *c* axis, similar to CaMnBi₂, suggests that an interlayer exchange interaction can be mediated by Dirac bands [11,18]. However, the questions remain: Is there any theoretical signature of coupling/entanglement with Dirac fermions in the magnetic excitation spectrum of YbMnBi₂? If so, is it significant enough to be measured in a neutron-scattering experiment?

Here, we present the results of inelastic neutron scattering (INS) measurements performed on YbMnBi₂ at four different temperatures, spanning the Néel temperature *T_N*. We show that the magnetic excitations are well-defined spin waves below *T_N*, becoming dispersive paramagnons (similar to spin waves) just above *T_N*, and the dispersion of both can be described with a local-moment Heisenberg model. In fitting the dynamical spin correlation function, we find that a good fit requires inclusion of a damping parameter γ , and that γ has no significant variation with momentum transfer \mathbf{Q} . While it is small, we note that no such damping is required in an insulating antiferromagnet such as CaMn₂Sb₂ [19]. To understand the nature of damping from particle-hole excitations associated with the Dirac dispersion that has been experimentally reported for YbMnBi₂ [16], we have evaluated a spin-fermion coupling model in the framework of the random phase approximation (RPA). The results show that the damping should be small in our case due to the vanishing density of states near the Dirac points, which suppresses the effects of the spin-fermion interaction, and is effectively independent of \mathbf{Q} . Thus, our observed damping is consistent

*sapkota@bnl.gov

†lclassen@bnl.gov

‡Present address: School of Physics, Chongqing University, Chongqing 400044, China.

§zaliznyak@bnl.gov

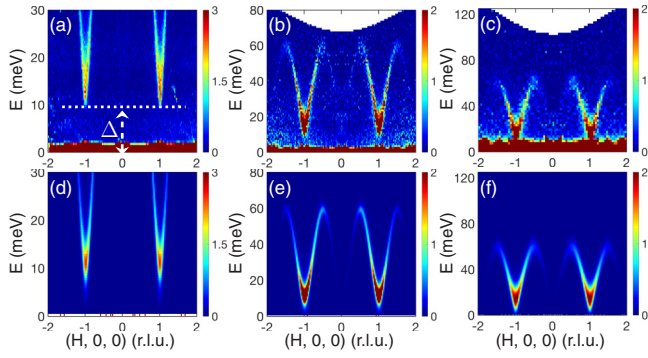


FIG. 1. Spin waves in YbMnBi₂ at $T = 4$ K. (a)–(c) INS spectra showing dispersion along the $[H, 0, 0]$ direction measured with incident energies $E_i = 35, 100,$ and 200 meV, respectively. The dashed line in (a) indicates the spin gap Δ (cf. Table I and Fig. S6). (d)–(f) INS spectra calculated using spin-wave dispersion and Eqs. (1) and (2), with the best fit parameters listed in Table I. Intensity scales shown in the color bars are in arbitrary units, which differ for different E_i .

with a coupling to Dirac electrons and allows us to determine the coupling constant, which is directly proportional to the experimental damping parameter.

Single crystals of YbMnBi₂ were grown from Bi flux as described in Ref. [12]. YbMnBi₂ orders antiferromagnetically below $T_N \approx 290$ K, with an ordered moment of $4.3 \mu_B$ at 4 K [12,13,20]. INS measurements were performed at SEQUOIA (Figs. 1–3) and HYSPEC [21] spectrometers at the Spallation Neutron Source, Oak Ridge National Laboratory. Four single crystals with a total mass of ≈ 1.8 g were coaligned in the $(H, 0, L)$ horizontal scattering plane, with the effective mosaic spread of $\lesssim 0.8^\circ$ full width at half maximum (FWHM). The measurements were carried out with incident energies $E_i = 35, 100,$ and 200 meV at $T = 4, 150, 270,$ and 320 K by rotating the sample about its vertical axis in 1° steps over a 270° range (70° for 150 K). Throughout this Rapid Communication, we index $\mathbf{Q} = (H, K, L)$ in reciprocal lattice units (r.l.u.) of the $P4/nmm$ lattice, $a = b = 4.48$ Å, $c = 10.8$ Å [12]. The collected event data were histogrammed into rectangular bins using the MANTID package [22]. For both the two-dimensional (2D) intensity maps (Figs. 1–3) and one-dimensional (1D) cuts (see Ref. [21]), the bin size of ± 0.0125 r.l.u. along $(H, 0, 0)$ and ± 0.05 r.l.u. along $(0, K, 0)$ was used, except for the 320-K data, for which it was ± 0.1 r.l.u. along $(0, K, 0)$; the bin size along $(0, 0, L)$ was ± 0.1 r.l.u.

Figures 1(a)–1(c) present INS spectra for YbMnBi₂ in the antiferromagnetic (AFM) phase at $T = 4$ K, which reveal the spin-wave dispersion along the $[H, 0, 0]$ symmetry direction. Magnetic excitations are well defined and sharp in both \mathbf{Q} and E , indicating the presence of conventional spin waves consistent with the local-moment description. The spin waves originate from the antiferromagnetic wave vector $\mathbf{Q}_{\text{AFM}} = (\pm 1, 0, 0)$, as expected for a Néel-type magnetic order in YbMnBi₂ [12]; the spin-gap $\Delta \sim 10$ meV marked in Fig. 1(a) is due to uniaxial anisotropy. The spin-wave dispersion bandwidth along $(H, 0, 0)$, $W = E_{\mathbf{Q}=(1.5,0,0)} - E_{\mathbf{Q}=(1,0,0)} \approx 50$ meV, is similar to the values measured in AMnBi₂ [18].

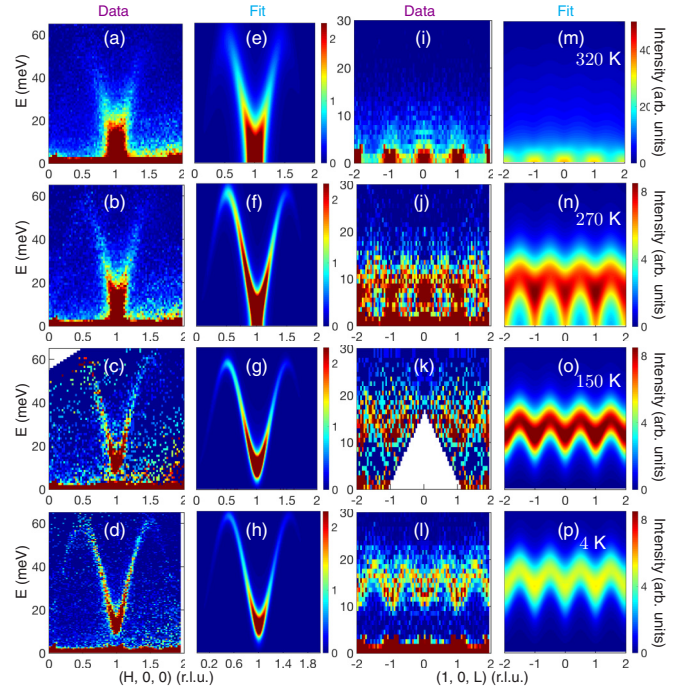


FIG. 2. INS spectra measured on YbMnBi₂ with $E_i = 100$ meV at $T = 320, 270, 150,$ and 4 K, illustrating the spin-wave dispersions along two symmetry directions, (a)–(d) $[H, 0, 0]$ and (i)–(l) $[0, 0, L]$. (e)–(h) and (m)–(p) INS spectra calculated using Eqs. (1) and (2) for the same wave vectors as the data, using the results of fits given in Table I, and corrected for the instrument resolution (see Ref. [21] for details).

To model the dispersion, we use a J_1 - J_2 - J_c Heisenberg model, where J_1 and J_2 are the nearest- and next-nearest-neighbor in-plane exchange interactions, respectively, and J_c is the interplane exchange. The dynamical spin correlation

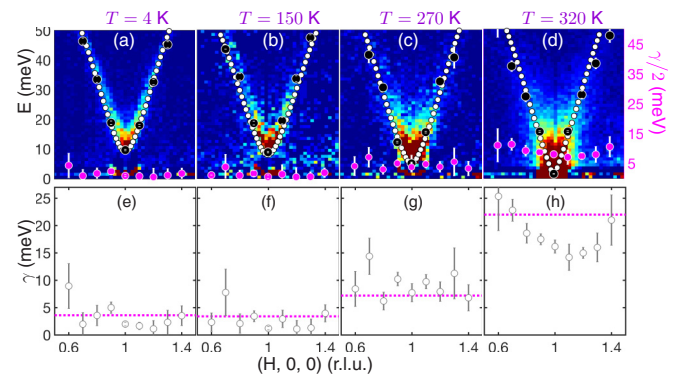


FIG. 3. (a)–(d) The damping parameter γ (magenta solid circles with white error bars) obtained from fitting 1D energy cuts using DHO response, and the low-energy part of spin-wave dispersion at $T = 4, 150, 270,$ and 320 K, respectively. Black circles show the corresponding spin-wave energy E_q which was fitted for all temperatures. White circles illustrate the dispersion obtained using the parameters in Table I for the corresponding temperature. The underdamped spin wave exists where $E_q > \gamma/2$. (e)–(h) Open circles are fitted values from 1D data and magenta dashed lines are for 2D data given in Table I. Error bars show one standard deviation.

TABLE I. Exchange coupling, uniaxial anisotropy, and damping parameters for YbMnBi₂ obtained from fitting two-dimensional data shown in Fig. 2.

	$T = 4$ K	$T = 150$ K	$T = 270$ K	$T = 320$ K
SJ_1 (meV)	25.9 ± 0.2	24.4 ± 0.3	27.1 ± 0.5	25.6 ± 0.6
SJ_2/SJ_1	0.39 ± 0.01	0.40 ± 0.01	0.43 ± 0.01	0.41 ± 0.01
$ SJ_c /SJ_1$	0.0050 ± 0.0001	0.0041 ± 0.0001	0.0022 ± 0.0001	0.0016 ± 0.0001
SD (meV)	-0.20 ± 0.01	-0.16 ± 0.01	-0.06 ± 0.02	-0.003 ± 0.001
Δ (meV)	9.1 ± 0.2	8.0 ± 0.2	5.3 ± 0.8	1 ± 1
γ (meV)	3.6 ± 0.2	3.4 ± 0.2	7 ± 1	22 ± 4

function $S(\mathbf{Q}, E)$ can be written as

$$S(\mathbf{q} + \mathbf{Q}_{\text{AFM}}, E) = S_{\text{eff}} \frac{(A_{\mathbf{q}} - B_{\mathbf{q}})}{E_{\mathbf{q}}} \frac{f_{\mathbf{q}}(E)}{1 - e^{-E/k_{\text{B}}T}}, \quad (1)$$

where S_{eff} is the effective fluctuating spin, k_{B} is the Boltzmann constant, and spin-wave theory gives $A_{\mathbf{q}} = 2S[2J_1 - 2J_2[\sin^2(\pi H) + \sin^2(\pi K)] - 2J_c \sin^2(\pi L) - D]$, $B_{\mathbf{q}} = 4SJ_1 \cos(\pi H) \cos(\pi K)$, and $E_{\mathbf{q}}^2 = A_{\mathbf{q}}^2 - B_{\mathbf{q}}^2$. In the absence of damping, the spectral function $f_{\mathbf{q}}(E) = \delta(E - E_{\mathbf{q}}) - \delta(E + E_{\mathbf{q}})$ describes the conservation of energy. In the presence of damping, which we introduce to obtain a good fit to the full intensity distribution, delta functions are replaced by Lorentzians [23] and the spectral function is given by the imaginary part of the dynamical susceptibility of a damped harmonic oscillator (DHO),

$$f_{\mathbf{q}}(E) = Z_{\mathbf{q}} \frac{2E_{\mathbf{q}}}{\pi} \frac{\gamma E}{[E^2 - E_{\mathbf{q}}^2]^2 + (\gamma E)^2}. \quad (2)$$

Here, γ is the damping parameter (Lorentzian FWHM) and prefactor $Z_{\mathbf{q}}$ ensures that the temperature-corrected DHO spectral function in Eq. (1) at all \mathbf{q} is normalized to 1 [for $(T, \gamma) \rightarrow 0, Z_{\mathbf{q}} \rightarrow 1$] [21].

We fit the data at each temperature using the cross section given by Eqs. (1) and (2) convolved with the instrumental resolution and accounting for the actual (\mathbf{Q}, E) binning of the data. The apparent energy width is dominated by the wave-vector resolution, which causes local averaging over the dispersion, so convolution with both the spectrometer resolution and binning functions is essential (additional details about the resolution correction and the fitting procedure are given in the Supplemental Material [21] and Refs. [24–29] therein). The resulting fits are shown side by side with the data in Figs. 1 and 2, and the best fit values thus obtained are listed in Table I. We find that the in-plane exchange parameters are nearly temperature independent. The gap Δ decreases with increasing temperature and approaches zero at $T \gtrsim T_{\text{N}}$.

Our central finding is a small but finite value of the damping parameter γ at all temperatures (Table I). It increases by roughly a factor of 6 in the paramagnetic state, just above T_{N} . While the global fits assume that γ is independent of \mathbf{Q} , we tested this assumption by fitting 1D energy cuts at different \mathbf{Q} values, as shown in Fig. 3; the corresponding plots of data with fits at 4 K and comparison calculations with $\gamma \sim 0$ are presented in Fig. S4 [21]. As one can see from Fig. 3, γ is non-negligible at all \mathbf{Q} and with no systematic variation with \mathbf{Q} (except possibly at $T > T_{\text{N}}$). The values are generally within 2σ of the global fit values from Table I, which are

indicated in the bottom panels of Fig. 3 by magenta dashed lines.

In order to understand the possible origin of the spin-wave damping, we first note that the contributions expected from magnon-magnon and magnon-defect scattering can be estimated by considering the case of the insulating antiferromagnetic layered compounds Rb₂MnF₄ [30] and CaMn₂Sb₂ [19]. In the first case, a high-resolution measurement of the magnon linewidths was performed, and the low-temperature ratio γ/W was at least an order of magnitude smaller than our result; in the latter case, any damping was smaller than resolution. We also note that coupling to two-magnon excitations cannot occur at energies below 2Δ , which is 18 meV in our case, and so such an effect is inconsistent with our observation of finite damping even at the lowest energies. Thus, we conclude that simple magnon-magnon interactions do not provide a plausible explanation of our results.

The decay of magnons into electron-hole excitations can have a very large effect in itinerant magnets [31–34]. The reason that similar effects are relatively small in our case is that unlike the parabolic dispersions of electrons in conventional metallic systems, the linear dispersion of Dirac fermions results in a vanishing density of states near the Dirac nodes, which suppresses the available phase space for spin-fermion interactions. In addition, the Dirac fermions and spin waves in YbMnBi₂ are spatially separated degrees of freedom that primarily propagate in different layers, which further inhibits the coupling. Hence, smaller broadening/damping with a very different nature (both energy and \mathbf{Q} dependence) than in metallic magnets should be expected.

Next, to establish that the spin-fermion coupling can indeed explain the observed non-negligible \mathbf{Q} -independent damping, we calculate the correction to the spin susceptibility through coupling to the Dirac fermions within RPA and show that the observed damping is consistent with theoretical expectations for YbMnBi₂. We model the system of spins and conduction electrons in YbMnBi₂ via the action

$$\begin{aligned}
S = & \int \frac{d^d p}{(2\pi)^d} \sum_{\eta=\pm} [\psi_{\eta}^{\dagger}(p)(ip_0 + \eta v_{1,\eta} \tau_x p_1 + v_{2,\eta} \tau_y p_2) \psi_{\eta}(p)] \\
& + \frac{g}{2} \int \frac{d^d p}{(2\pi)^d} \int \frac{d^d q}{(2\pi)^d} \\
& \times [S_{\mathbf{q}} \psi_{+}^{\dagger}(p) \boldsymbol{\sigma} \otimes \tau_x \psi_{-}(p - q) + \text{H.c.}] \\
& + \int \frac{d^d q}{(2\pi)^d} S_{\mathbf{q}} \chi_0^{-1} S_{-\mathbf{q}}, \quad (3)
\end{aligned}$$

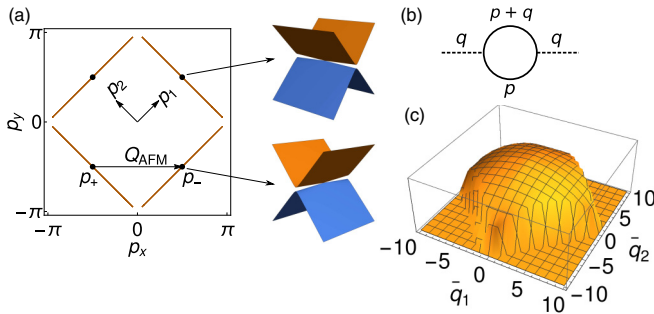


FIG. 4. (a) The Fermi surface resulting from the anisotropic Dirac cones and a shift of the crossing away from the Fermi surface. The Dirac cones are rotated with respect to each other as sketched to the right. The centers of the \mathbf{p}_+ and \mathbf{p}_- cones are connected by the antiferromagnetic wave vector $\mathbf{Q}_{\text{AFM}} = (\pi, 0)$. (b) Diagrammatic representation of the leading correction to the spin susceptibility through coupling to the Dirac electrons. Solid lines are Dirac propagators, and dashed lines are spin waves. (c) The polarization $\text{Im } \Pi(E, \bar{q}_1, \bar{q}_2)$ obtained by numerical integration for an energy $E > \sqrt{2}v_{\parallel}q$ and $v_{\parallel}/v_{\perp} = 0.005$ as a function of $\bar{q}_i = v_{\perp}q_i$.

which describes two Dirac cones at \mathbf{p}_{η} [$\eta = \pm$; see Fig. 4(a)] with anisotropic velocities $v_{1,+} = v_{2,-} = v_{\perp}$ and $v_{1,-} = v_{2,+} = v_{\parallel}$ rotated with respect to each other ($v_{\parallel}/v_{\perp} \approx 0.005$ in YbMnBi_2) [16]. We use rotated coordinates $p_{1,2} = (p_x \pm p_y)/\sqrt{2}$. Pauli matrices (τ) σ act on (pseudo)spin, respectively. The Mn spin waves are represented by the three-component boson field \mathbf{S} . Their dynamical susceptibility is given by the bare expression, without damping, $\chi_0^{-1}(E) = E^2 - E_q^2$ [cf. Eq. (2)].

For simplicity, we perform calculations at $T = 0$ and in $d = 2 + 1$ dimensions. We assume that the Dirac points have opposite chirality, as was found in the related compound SrMnBi_2 [35], and we consider a coupling αg which does not break chiral symmetry. In the coupling term in Eq. (3), we measure the wave-vector transfer relative to the antiferromagnetic wave vector, $\mathbf{Q}_{\text{AFM}} = \mathbf{p}_+ - \mathbf{p}_-$, which happens to connect the centers of the Dirac cones [see Fig. 4(a)]. Because of the large anisotropy, $v_{\perp} \approx 9 \text{ eV \AA}$ and $v_{\parallel} \approx 0.043 \text{ eV \AA}$ in YbMnBi_2 [16,17], the elliptical Fermi surface is extremely elongated and appears very similar to a true nodal line.

The leading correction to the bare susceptibility due to coupling to the Dirac electrons renormalizes the spin susceptibility via the polarization $\chi^{-1} = \chi_0^{-1} - \Pi$ [Fig. 4(b)]. As the coupling is small and the semimetallic state in 2D Dirac materials is known to be stable due to a vanishing density of states at the Dirac points, we expect the second-order approximation for Π to adequately capture the damping effects,

$$\Pi(E, \mathbf{q}) = -\frac{g^2}{2} \int \frac{d^d p}{(2\pi)^d} \text{Tr}[G_+(p_0, \mathbf{p}) \times \tau_x G_-(p_0 + E, \mathbf{p} + \mathbf{q}) \tau_x], \quad (4)$$

with Dirac propagators $G_{\eta}(p_0, \mathbf{p}) = (-ip_0 + \eta v_{1,\eta} \tau_x p_1 + v_{2,\eta} \tau_y p_2) / (p_0^2 + v_{1,\eta}^2 p_1^2 + v_{2,\eta}^2 p_2^2)$. The damping can be determined by the imaginary part of the retarded polarization after analytical continuation, $ip_0 \rightarrow E + i0^+$. For general v_{\perp}, v_{\parallel} ,

we obtain a lengthy expression, which can be found in the Supplemental Material [21].

It is instructive to consider two limits. For isotropic Dirac cones, $v_{\perp} = v_{\parallel} = v_F$, we find

$$\text{Im } \Pi^R(E, \mathbf{q}) = \frac{N_f}{8v_F^2} g^2 \text{sgn}(E) \sqrt{E^2 - v_F^2 \mathbf{q}^2} \Theta(E^2 - v_F^2 \mathbf{q}^2), \quad (5)$$

where N_f is the number of Dirac cone pairs and Θ is the step function. There are four Dirac points in each Brillouin zone of YbMnBi_2 [16,17], so $N_f = 2$. Although Eq. (5) has approximately the correct functional form for the DHO ($\text{Im } \Pi^R \approx cE$), the kinematic constraint $E > v_F |\mathbf{q}|$ usually cannot be satisfied because for most wave vectors, electronic energies are much larger than the spin-wave energy. For $E^2 < v_F^2 \mathbf{q}^2$, the polarization function is purely real [36].

The extreme anisotropy of the electronic dispersion in YbMnBi_2 relaxes the kinematic constraint. For momentum transfers along \mathbf{Q}_{AFM} , corresponding to the data shown in Figs. 1–3, the leading order in small (v_{\parallel}/v_{\perp}) reads

$$\text{Im } \Pi^R(E, q) \approx \frac{N_f}{2\pi v_{\perp}^2} g^2 E \Theta(E^2 - 2v_{\parallel}^2 q^2). \quad (6)$$

Accounting for further corrections leads to a weak momentum dependence [21]. The full numerical result for $\text{Im } \Pi^R$ is presented in Fig. 4. The main processes responsible for the enabled damping connect points along the elongated Fermi surfaces so that their energy cost is determined by v_{\parallel} . Due to its remarkable smallness, spin waves are able to excite such particle-hole pairs.

We conclude that the spin-wave damping factor in Eq. (2) is given by $\gamma \approx N_f g^2 / (2\pi v_{\perp}^2)$. Thus, using $\gamma \approx 3.6 \text{ meV}$ (Table I), $N_f = 2$, $v_F = 9 \text{ eV \AA}$, we can estimate the coupling constant, $g \approx 1.0 \text{ eV}^{3/2} \text{ \AA}$. The obtained value of g quantifies the spin-fermion interaction in YbMnBi_2 and can be used, in future work, to analyze the effect of magnetism on the transport of Dirac electrons in the framework of Eq. (3).

In summary, we measured magnetic excitations in the Dirac material YbMnBi_2 for temperatures in the range of $0.02 \leq T/T_N \leq 1.10$. The results show dispersing spin waves for all temperatures and their detailed analysis unfolds the nature of spin-fermion coupling between the magnetic Mn layer and Dirac fermions of the Bi layer. We find a small, but distinct, damping of spin waves, which for $T < T_N$ is weakly dependent on temperature and is nearly independent of wave vector. Despite its small magnitude, the observed damping indicates a substantial spin-fermion coupling parameter, $g \approx 1.0 \text{ eV}^{3/2} \text{ \AA}$, which we quantify by comparing the experiment with the theoretical analysis of the model action for Dirac fermions coupled to spin waves [Eq. (3)]. Therefore, by combining the experimental measurements and theory, we establish the existence of long-sought significant spin-fermion coupling in the 112 family of Dirac materials.

We thank Alexei Tsvetlik and Michael Scherer for helpful comments and discussions. The work at Brookhaven National Laboratory was supported by the Office of Basic Energy Sciences, Materials Sciences and Engineering

Division, U.S. Department of Energy (DOE) under Contract No. DE-SC0012704. This research used resources at the Spallation Neutron Source, a DOE Office of Science User

Facility operated by the Oak Ridge National Laboratory. L.C. acknowledges funding from a Feodor-Lynen research fellowship of the Alexander von Humboldt Foundation.

- [1] T. Wehling, A. Black-Schaffer, and A. Balatsky, *Adv. Phys.* **63**, 1 (2014).
- [2] M. Khodas, I. A. Zaliznyak, and D. E. Kharzeev, *Phys. Rev. B* **80**, 125428 (2009).
- [3] K. Wang, D. Graf, H. Lei, S. W. Tozer, and C. Petrovic, *Phys. Rev. B* **84**, 220401(R) (2011).
- [4] A. Wang, D. Graf, L. Wu, K. Wang, E. Bozin, Y. Zhu, and C. Petrovic, *Phys. Rev. B* **94**, 125118 (2016).
- [5] Y. Zhang, Y.-W. Tan, H.-L. Stormer, and P. Kim, *Nature (London)* **438**, 201 (2005).
- [6] M. Z. Hasan and C. L. Kane, *Rev. Mod. Phys.* **82**, 3045 (2010).
- [7] F. Katmis, V. Lauter, F. S. Nogueira, B. A. Assaf, M. E. Jamer, P. Wei, B. Satpati, J. W. Freeland, I. Eremin, D. Heiman, P. Jarillo-Herrero, and J. S. Moodera, *Nature (London)* **533**, 513 (2016).
- [8] H. Masuda, H. Sakai, M. Tokunaga, Y. Yamasaki, A. Miyake, J. Shiogai, S. Nakamura, S. Awaji, A. Tsukazaki, H. Nakao, Y. Murakami, T.-h. Arima, Y. Tokura, and S. Ishiwata, *Sci. Adv.* **2**, e1501117 (2016).
- [9] J. Park, G. Lee, F. Wolff-Fabris, Y. Y. Koh, M. J. Eom, Y. K. Kim, M. A. Farhan, Y. J. Jo, C. Kim, J. H. Shim, and J. S. Kim, *Phys. Rev. Lett.* **107**, 126402 (2011).
- [10] A. Zhang, C. Liu, C. Yi, G. Zhao, T.-l. Xia, J. Ji, Y. Shi, R. Yu, X. Wang, C. Chen, and Q. Zhang, *Nat. Commun.* **7**, 13833 (2016).
- [11] Y. F. Guo, A. J. Princep, X. Zhang, P. Manuel, D. Khalyavin, I. I. Mazin, Y. G. Shi, and A. T. Boothroyd, *Phys. Rev. B* **90**, 075120 (2014).
- [12] A. Wang, I. Zaliznyak, W. Ren, L. Wu, D. Graf, V. O. Garlea, J. B. Warren, E. Bozin, Y. Zhu, and C. Petrovic, *Phys. Rev. B* **94**, 165161 (2016).
- [13] K. Wang, D. Graf, L. Wang, H. Lei, S. W. Tozer, and C. Petrovic, *Phys. Rev. B* **85**, 041101(R) (2012).
- [14] S. O. Diallo, V. P. Antropov, T. G. Perring, C. Broholm, J. J. Pulikkotil, N. Ni, S. L. Bud'ko, P. C. Canfield, A. Kreyssig, A. I. Goldman, and R. J. McQueeney, *Phys. Rev. Lett.* **102**, 187206 (2009).
- [15] M. Chinotti, A. Pal, W. J. Ren, C. Petrovic, and L. Degiorgi, *Phys. Rev. B* **94**, 245101 (2016).
- [16] S. Borisenko, D. Evtushinsky, Q. Gibson, A. Yaresko, K. Koepfner, T. Kim, M. Ali, J. van den Brink, M. Hoesch, A. Fedorov, E. Haubold, Y. Kushnirenko, I. Soldatov, R. Schäfer, and R. J. Cava, *Nature Commun.* **10**, 3424 (2019).
- [17] D. Chaudhuri, B. Cheng, A. Yaresko, Q. D. Gibson, R. J. Cava, and N. P. Armitage, *Phys. Rev. B* **96**, 075151 (2017).
- [18] M. C. Rahn, A. J. Princep, A. Piovano, J. Kulda, Y. F. Guo, Y. G. Shi, and A. T. Boothroyd, *Phys. Rev. B* **95**, 134405 (2017).
- [19] D. E. McNally, J. W. Simonson, J. J. Kistner-Morris, G. J. Smith, J. E. Hassinger, L. DeBeer-Schmitt, A. I. Kolesnikov, I. A. Zaliznyak, and M. C. Aronson, *Phys. Rev. B* **91**, 180407(R) (2015).
- [20] I. A. Zaliznyak, A. T. Savici, V. O. Garlea, B. Winn, U. Filges, J. Schneeloch, J. M. Tranquada, G. Gu, A. Wang, and C. Petrovic, *J. Phys.: Conf. Ser.* **862**, 012030 (2017).
- [21] See Supplemental Material at <http://link.aps.org/supplemental/10.1103/PhysRevB.101.041111> for additional details, which includes Refs. [24–29].
- [22] O. Arnold, J. Bilheux, J. Borreguero, A. Buts, S. Campbell, L. Chapon, M. Doucet, N. Draper, R. F. Leal, M. Gigg, V. Lynch, A. Markvardsen, D. Mikkelsen, R. Mikkelsen, R. Miller, K. Palmen, P. Parker, G. Passos, T. Perring, P. Peterson, S. Ren, M. Reuter, A. Savici, J. Taylor, R. Taylor, R. Tolchenov, W. Zhou, and J. Zikovsky, *Nucl. Instrum. Methods Phys. Res., Sect. A* **764**, 156 (2014).
- [23] I. A. Zaliznyak, L.-P. Regnault, and D. Petitgrand, *Phys. Rev. B* **50**, 15824 (1994).
- [24] G. L. Squires, *Introduction to the Theory of Thermal Neutron Scattering*, 3rd ed. (Cambridge University Press, Cambridge, UK, 2012).
- [25] I. A. Zaliznyak and S.-H. Lee, in *Modern Techniques for Characterizing Magnetic Materials*, edited by Y. Zhu (Springer, New York, 2005), pp. 3–64.
- [26] I. Zaliznyak, A. T. Savici, M. Lumsden, A. Tsvetlik, R. Hu, and C. Petrovic, *Proc. Natl. Acad. Sci. USA* **112**, 10316 (2015).
- [27] J. Lamsal and W. Montfrooij, *Phys. Rev. B* **93**, 214513 (2016).
- [28] G. Ehlers, A. A. Podlesnyak, J. L. Niedziela, E. B. Iverson, and P. E. Sokol, *Rev. Sci. Instrum.* **82**, 085108 (2011).
- [29] D. L. Abernathy, M. B. Stone, M. J. Loguillo, M. S. Lucas, O. Delaire, X. Tang, J. Y. Y. Lin, and B. Fultz, *Rev. Sci. Instrum.* **83**, 015114 (2012).
- [30] S. P. Bayrakci, D. A. Tennant, P. Leininger, T. Keller, M. C. R. Gibson, S. D. Wilson, R. J. Birgeneau, and B. Keimer, *Phys. Rev. Lett.* **111**, 017204 (2013).
- [31] S. O. Diallo, D. K. Pratt, R. M. Fernandes, W. Tian, J. L. Zarestky, M. Lumsden, T. G. Perring, C. L. Broholm, N. Ni, S. L. Bud'ko, P. C. Canfield, H.-F. Li, D. Vaknin, A. Kreyssig, A. I. Goldman, and R. J. McQueeney, *Phys. Rev. B* **81**, 214407 (2010).
- [32] A. Sapkota, B. G. Ueland, V. K. Anand, N. S. Sangeetha, D. L. Abernathy, M. B. Stone, J. L. Niedziela, D. C. Johnston, A. Kreyssig, A. I. Goldman, and R. J. McQueeney, *Phys. Rev. Lett.* **119**, 147201 (2017).
- [33] A. Sapkota, P. Das, A. E. Böhrer, B. G. Ueland, D. L. Abernathy, S. L. Bud'ko, P. C. Canfield, A. Kreyssig, A. I. Goldman, and R. J. McQueeney, *Phys. Rev. B* **97**, 174519 (2018).
- [34] W. Jayasekara, Y. Lee, A. Pandey, G. S. Tucker, A. Sapkota, J. Lamsal, S. Calder, D. L. Abernathy, J. L. Niedziela, B. N. Harmon, A. Kreyssig, D. Vaknin, D. C. Johnston, A. I. Goldman, and R. J. McQueeney, *Phys. Rev. Lett.* **111**, 157001 (2013).
- [35] G. Lee, M. A. Farhan, J. S. Kim, and J. H. Shim, *Phys. Rev. B* **87**, 245104 (2013).
- [36] J. González, F. Guinea, and M. A. H. Vozmediano, *Phys. Rev. Lett.* **77**, 3589 (1996).